PHYSICAL REVIEW E **108**, L062601 (2023)

Letter

Emergent structures in active block copolymer composites

Javier Díaz and Ignacio Pagonabarraga[*]
Departament de Física de la Matèria Condensada, Universitat de Barcelona, Martí i Franquès 1, 08028 Barcelona, Spain
and Universitat de Barcelona Institute of Complex Systems (UBICS), Universitat de Barcelona, 08028 Barcelona, Spain

(Received 21 March 2023; accepted 9 November 2023; published 11 December 2023)

Block copolymer melts offer unique templates to control the position and alignment of nanoparticles due to their ability to self-assemble into periodic ordered structures. Active particles are shown to coassemble with block copolymers leading to emergent organized structures. The block copolymer acts as a soft template that can control the self-propulsion of active particles, both for interface-segregated and selective nanoparticles. At moderate activities, active particles can form organized structures such as polarized trains or rotating vortices. At high activity, the contrast in the polymeric and colloidal timescales can lead to particle swarms with distorted block copolymer morphology, due to the competition between polymeric self-assembly and active Brownian self-propulsion.

DOI: 10.1103/PhysRevE.108.L062601

Block copolymer (BCP) melts are ideal matrices to template the location of passive nanoparticles (NPs), due to their ability to self-assemble into ordered mesophases [1–4], such as lamellae or hexagonally ordered cylinders, because of the heterogeneity of the BCP chain. Passive particles have been shown to form ordered structures when miscible with one of the BCP phases [5–7], or decorating the interface [4]. Furthermore, NPs can induce an order-to-order transition in the BCP morphology [8,9], indicating that BCP melts not only control the NP location, but that they are responsive to the fillers' presence.

Active particles (APs) are intrinsically out of equilibrium, as they consume energy from the surrounding medium to produce work. This work can be used, for instance, to allow particles to self-propel with a given direction. Suspensions of self-propelled particles have been shown to display a rich phase behavior [10–19].

AP dispersions in a complex medium have resulted in emergent organized structures [20,21], such as the accumulation of APs at hard confining walls, the emergence of collective motion for active agents embedded in smectic liquid crystals [22], or the formation of vortices of APs under circular confinement [23–27]. Soft confinement, instead, allows APs to deform the confining medium, such as the case of active filaments within vesicles [28,29]. The geometry of obstacles or confinement has been shown to play a role in the accumulation of APs in curved walls [30–32]. Furthermore, inhomogeneous media can lead to the localization of APs in the absence of hard confinement [33]. BCP melts constitute a class of deformable confining media and, due to their intrinsic mesoscale ordering, can control the APs' dispersion, which will be shown to lead to the emergence of coassembled BCP/AP morphologies.

Active Janus particles at air/water interfaces have been shown to enhance their active persistence length by reducing their rotational diffusivity [34], driven by the wetting of the particle [35]. While equilibrated flat air/water interfaces have been used to study the constrained collective behavior of APs, in this Letter we exploit the intrinsic structure of the BCP interface. NPs with chemically inhomogeneous surfaces have been successfully dispersed within BCP melts, leading to their anchoring at interfaces [36–38].

We will address the coassembly between APs and BCP melt mesophases, and their ability to induce new BCP structures. In order to capture the overall phase behavior of APs in BCP melts, we use a mesoscopic hybrid model that allows us to reach relatively large length scales and timescales [39]. The total free energy of the system is decomposed as $F_{\rm tot} = F_{\rm pol} + F_{\rm cpl} + F_{\rm cc}$, where $F_{\rm pol}$ is the standard Ohta-Kawasaki [40] continuous description of a BCP melt via the differences in the concentration of A and B monomers $\psi = \phi_A - \phi_B + (1 - 2f_0)$, with f_0 the overall melt composition. The colloid-colloid contribution $F_{\rm cc}$ is a pairwise additive potential that prevents overlapping between APs. Colloids and polymers are coupled through the interaction term $F_{\rm cpl} = \sum_i \sigma \int d\mathbf{r}\psi_c(r)[\psi - \psi_0]^2$ which introduces a coupling energetic scale σ and a chemical affinity parameter ψ_0 that specifies the AP relative solubility with the BCP. The shape and size of the particle is controlled by the tagged function ψ_c [41].

The dynamics of a two-dimensional system of N_p APs with radius R is described via the overdamped Langevin equations

$$\frac{d\mathbf{r}_i}{dt} = v_a\hat{\mathbf{n}}_i + \gamma_t^{-1}\left(\mathbf{f}_i^{\rm cc} + \mathbf{f}_i^{\rm cpl}\right) + \sqrt{2D_t}\xi_t, \tag{1a}$$

$$\frac{d\phi_i}{dt} = \gamma_r^{-1}\left(M_i^{\rm cc} + M_i^{\rm cpl}\right) + \sqrt{2D_r}\xi_r, \tag{1b}$$

for the translational, $\mathbf{r}_i$, and orientational, ϕ_i, degrees of freedom of particle i, respectively. Forces, $\mathbf{f}_i$, and torques, M_i, are derived from the colloid-colloid and coupling contributions to the free energy. The Einstein relation applies for both the

---

[*] ipagonabarraga@ub.edu

translational, D_t, and rotational, D_r, diffusion constants, while random noises ξ_t and ξ_r satisfy the fluctuation-dissipation theorem. Each AP self-propels with velocity v_a with the direction given by $\hat{\mathbf{n}}_i = (\cos\phi_i, \sin\phi_i)$, which decorrelates in a rotational diffusion timescale $t_{\text{rot}} = D_r^{-1}$. It can be compared with the timescale in which an AP moves its diameter, $t_{\text{swim}} = 2R/v_a$, to define the Péclet number, $\text{Pe} = t_{\text{rot}}/t_{\text{swim}}$. Similarly, the persistence length, $l_{\text{pers}} = v_a t_{\text{rot}}$, is the distance that the particle displaces before decorrelating its orientation. The ratio, $\tilde{\epsilon}_{\text{cpl}} \equiv \epsilon_{\text{cpl}}/\epsilon_{\text{swim}}$, between the typical swimming energy $\epsilon_{\text{swim}} = 2Rv_a\gamma_t$ and the BCP coupling energy $\epsilon_{\text{cpl}} = \pi R^2\sigma$ can be understood as a Bond number that quantifies the AP ability to deform the BCP interfaces and escape from them. The packing fraction of APs in an area $V = L_x \times L_y$ is $\phi_p = N_p\pi R^2/V$.

Polar aligning interactions in active matter have been widely modeled using the Vicsek model [42], which predicts the flocking transition for APs. We introduce a Vicsek-like torque, $M_i^{\text{cc}} = K_{\text{cc}}/(\pi R_{\text{cc}}^2)\sum_j \sin(\phi_i - \phi_j)$, where particle i interacts with neighbors j within a cutoff distance $R_{\text{cc}} = 4R$ [43]. Similarly, a torque can be introduced to couple the orientation of APs with the BCP interface as $M_i^{\text{cpl}} = -K_{\text{cpl}}/(\pi R^2)\partial/\partial\phi_i \int_{r<R} d\mathbf{r}(\nabla\psi\cdot\hat{\mathbf{n}}_i)^2$, to capture the alignment of APs under confinement [44]. The magnitudes of these two types of torques can be quantified through the dimensionless parameters, $g_{\text{cc}} = K_{\text{cc}}/(\pi R_{\text{cc}}^2 k_B T)$ and $g_{\text{cpl}} = K_{\text{cpl}}/(\pi R^2 k_B T)$, for particle-particle and coupling contributions, respectively.

The Cahn-Hilliard equation [45,46] controls the time evolution of the BCP order parameter $\partial\psi/\partial t = M\nabla^2(\delta F_{\text{tot}}/\delta\psi)$ that drives the phase separation into ordered structures. The BCP diffusive timescale, $t_{\text{BCP}} \propto M^{-1}$, depends on the mobility M, which can be compared with the AP swimming time through the ratio $t_{\text{rel}} = t_{\text{BCP}}/t_{\text{swim}} = (t_{\text{BCP}}/t_{\text{rot}})\text{Pe}$. In this work, we will fix the equilibrium system parameters and modify the Pe and AP concentration ϕ_p, therefore exploring different $\tilde{\epsilon}_{\text{cpl}} \propto \text{Pe}^{-1}$ and $t_{\text{rel}} \propto \text{Pe}$ regimes. We select R and t_{rot} as the units of length and time, respectively. We consider a BCP in the strong segregation regime with a Flory-Huggins parameter [40] $\chi N \approx 89.3$; a complete description of the model and the relevant parameters can be found in the Supplemental Material [47].

Several observables are used to quantify the phase behavior of the system. The nematic order parameter $S_{\text{cpl}} = \langle 2(\hat{\mathbf{n}}_i \cdot \nabla\psi)^2 - 1\rangle$ couples the AP orientation with the vector pointing perpendicular to the interface, $\nabla\psi$. Since the spatial inhomogeneity introduced by the BCP mesophase can prevent global polar ordering, the system polarization is obtained as the average, $P_{\text{cc}} = \langle P_{\text{cc}}^i\rangle$, of the local polar order for particle i defined as $P_{\text{cc}}^i = 1/N_i\sum_{j=1}^{N_i}\hat{\mathbf{n}}_i\cdot\hat{\mathbf{n}}_j$ for N_i neighbors of particle i within a distance $r_{ij} < 1.3(2R)$ based on the radial distribution function. Similarly, the nematic particle-particle alignment is characterized as $S_{\text{rel}} = \langle S_{\text{rel}}^i\rangle$ with $S_{\text{rel}}^i = 1/N_i\sum_{j=1}^{N_i} 2(\hat{\mathbf{r}}_{ij}\cdot\hat{\mathbf{n}}_j)^2 - 1$, which allows us to distinguish different types of in-cluster alignment. The fraction of all APs located at the BCP interface is quantified as Φ. Additionally, cluster analysis allows us to calculate the fraction Φ_{1D} of AP clusters with one-dimensional (1D)-like structures [12] [see Eq. (S27) [47]] and the fraction $\Phi_{\text{circle}}^{\text{BCP}}$ of BCP domains with an approximately circular shape [see Eq. (S29) [47]].

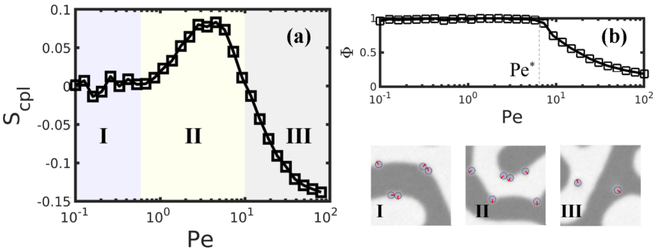

FIG. 1. Assembly of neutral APs in the dilute regime ($\phi_p = 0.01$) without alignment torques. In (a) the nematic coupling order parameter S_{cpl} is shown vs the Péclet number Pe. (b) shows the fraction of APs at the interface, Φ. At the bottom right we can see representative small detailed snapshots of each regime showing AP's orientation as red arrows. Full system videos of each regime can be found in the Supplemental Material [47] and are described in Table S1.

NPs with a neutral interaction with both segments of the BCP (surfactantlike, with $\psi_0 = 0$) anchor at the BCP melt interfaces [4]. Figure 1 displays APs ordering in terms of Pe, in a symmetric lamellar-forming BCP with a periodicity $H_0/R = 11.2$. No alignment torques are introduced either through the particle-polymer coupling $g_{\text{cpl}} = 0$ or the particle-particle polar alignment $g_{\text{cc}} = 0$. At low concentrations, $\phi_p = 0.01$, APs can acquire both orientational and translational order, with three distinguishable regimes: (I) Passivelike APs with low activity, $\text{Pe} < 1$, display no defined nematic order with respect to the interface, $S_{\text{cpl}} \sim 0$, while anchoring at the interface $\Phi \sim 1$. (II) Moderately active APs with $1 < \text{Pe} < 10$ can self-propel along the interface before encountering a lamellar defect. APs that accumulate at lamellar defects contribute to positive nematic order, which couples the APs' direction and the interface normal $S_{\text{cpl}} > 0$, while the APs remain at the interface $\Phi \sim 1$. (III) We observe APs detaching from the interface for small energy ratios, below a critical value $\tilde{\epsilon}_{\text{cpl}}^* \approx 21.5$ where the swimming energy is considerably larger than the coupling energy, which corresponds to $\text{Pe} > 10$, as shown in Fig. S3 [47]. Furthermore, as the activity grows, APs develop a stronger tangential orientation with respect to the interfaces, with $S_{\text{cpl}} < 0$. This occurs because APs that collide with the interface with a tangential orientation ($S_{\text{cpl}} < 0$) are more likely to remain at the interface for longer times than APs colliding *head on* ($S_{\text{cpl}} > 0$), due to the component of the active velocity projected onto the interface.

The accumulation of APs at lamellar defects and their nematic ordering in regime (II) is a consequence of the fingertiplike morphology of symmetric BCP, which allows APs to accumulate at high-curvature regions of the interface. In the absence of defects, i.e., an equilibrated phase, the lamellar morphology displays no nematic order, while BCP mesophases with an intrinsic curvature feature an increased peak in positive nematic ordering, as shown in Fig. S2 [47]. Hence, heterogeneities in complex, soft templates play a central role, leading to the coassembly of APs within BCP melts.

At moderate concentrations, AP collective behavior emerges [29]. Figure 2 shows AP phase behavior as a function of APs' concentrations ϕ_p and Pe, in the presence of a strong particle-interface $g_{\text{cpl}} = 34.9$, moderate particle-particle coupling $g_{\text{cc}} = 0.06$ alignment, in order to mimic the

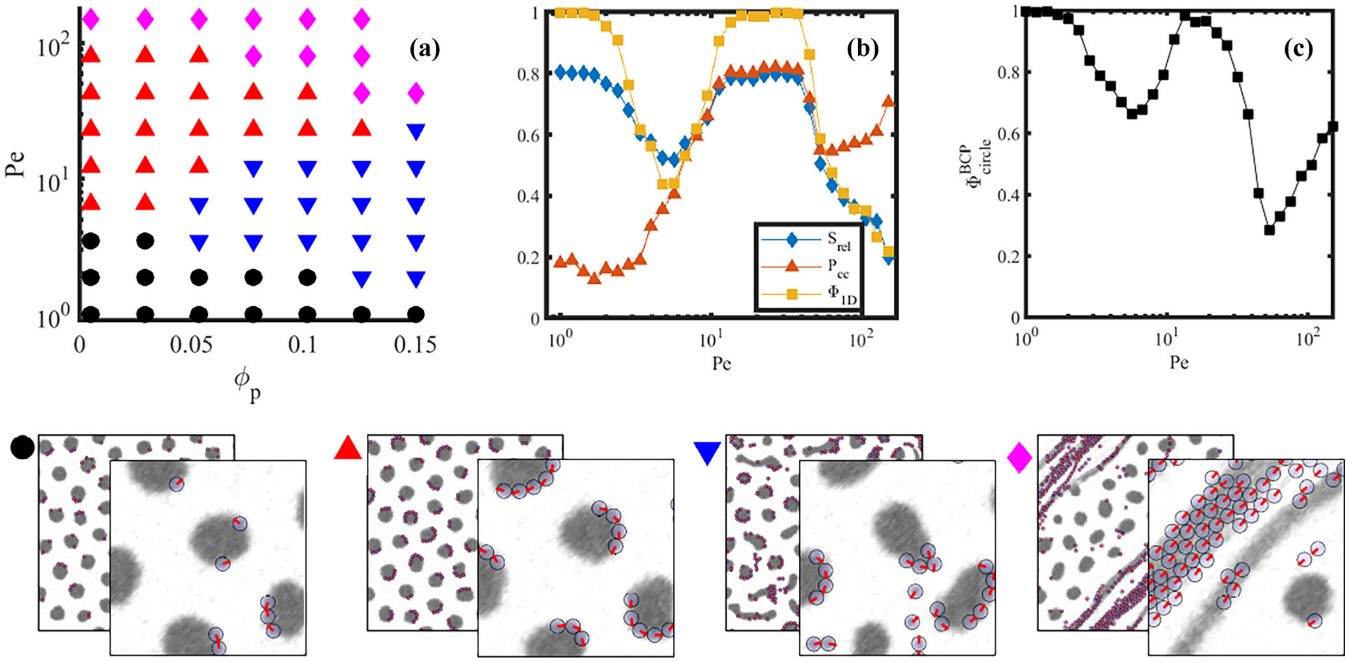

FIG. 2. Phase behavior of neutral APs with coupling alignment between APs and BCP $g_{cpl} = 34.9$ and APs' polar alignment $g_{cc} = 0.06$, in (a). Phases are marked as passivelike in black circles, downward blue triangles for unstructured clusters, upward red triangles for polarized trains, and diamonds for swarms escaped from the interface. In (b) and (c) S_{rel}, P_{cc}, Φ_{1D}, and Φ^{BCP}_{circle} are shown for a fixed concentration $\phi_p = 0.088$. Representative snapshots of each regime are shown at the bottom with the top-left marker indicating the corresponding regime.

alignment interaction experienced by explicitly anisotropic APs [29]. We consider an asymmetric BCP, $f_0 = 0.3$ with periodicity $H_0/R = 15.0$. Neutral APs segregate toward the interface of circle-forming BCP domains, with the system being initialized with APs at the interface of an already-equilibrated BCP. Several regimes can be distinguished in Fig. 2(a). The curves of S_{rel}, P_{cc}, and Φ_{1D} are shown in Fig. 2(b) and Φ^{BCP}_{circle}, for a fixed AP concentration $\phi_p = 0.088$, which are used to determine the dynamical regimes in the system.

As shown in Fig. 2(a), at low Pe APs move along the interface before encountering an additional AP (marked as black circles), leading to colloidal aggregation at the interface, similar to the accumulation mechanism described in Fig. 1. This low activity region is characterized by interfacial 1D clusters, with $\Phi_{1D} \sim 1$, and high nematic $S_{rel} \sim 0.8$ but low polar $P_{cc} \sim 0.2$ interparticle alignment [Fig. 2(b)] due to the low g_{cc} coupling. The BCP morphology remains circular, as shown in Fig. 2(c).

Higher Pe allows APs to overcome the energetic interfacial barrier and escape into the bulk (marked as blue and red triangular symbols), with a minimum activity rate that decreases with ϕ_p. Two regimes can be distinguished: First, unstructured clusters (marked as downward blue triangles) are found for larger concentrations and moderate activity, where APs possess enough active energy to escape the interface but, upon entering the bulk regions, tend to form unstructured clusters characterized by a decrease in P_{cc}, Φ_{1D}, and S_{rel}, as shown in Fig. 2(b). The relatively high local concentration and the moderate activity promote aggregation, which introduces considerable changes in the BCP mesophases, as shown in the decrease in circular BCP domains in Fig. 2(c).

Second, as shown in Fig. 2(a), for moderate activities but lower concentrations, APs can form polarized 1D clusters that maintain a continuous flow along the interface (marked as red upward triangles). In this regime, APs have enough active energy not only to escape from the interface, but also to self-propel through the bulk before entering another BCP domain. This process can be repeated leading to the formation of polarized trainlike clusters, characterized with high polarization in Fig. 2(b). The short-time dynamics of both trainlike and unstructured cluster regimes are considerably similar, as depicted in Fig. 3, where a transient regime of low Φ_{1D} is observed. Nonetheless, at a higher activity rate (Pe = 11, red upward triangles) APs are able to enter new BCP interfaces and form 1D polarized trains, while lower activity promotes the formation of unstructured clusters (Pe = 6, blue downward triangles).

Finally, for considerably large activity, APs completely detach from the interface, as depicted at the top of the phase diagram in Fig. 2(a). APs can reorient upon collisions to form polarized clusters (blue diamonds) which leads to high polarization but low interface-coupled nematic order, as displayed in Fig. 2(b). In this regime activity decouples the BCP and AP dynamics, signaled by the timescale ratio t_{rel}, for varying activity, where BCP relaxation cannot accommodate the fast AP dynamics. In Fig. 2(c) the BCP mesophase is largely distorted as APs are able to penetrate the interface, leading to a pronounced decrease in the fraction of circular domains for Pe ~ 50, followed by an increase in Φ^{BCP}_{circle} indicating the recovery of the equilibrium circular phase as the dynamics of the BCP and APs decouple.

As opposed to neutral NPs, selective ones ($\psi_0 = -1$) are miscible in one of the mesosocopic domains formed by the

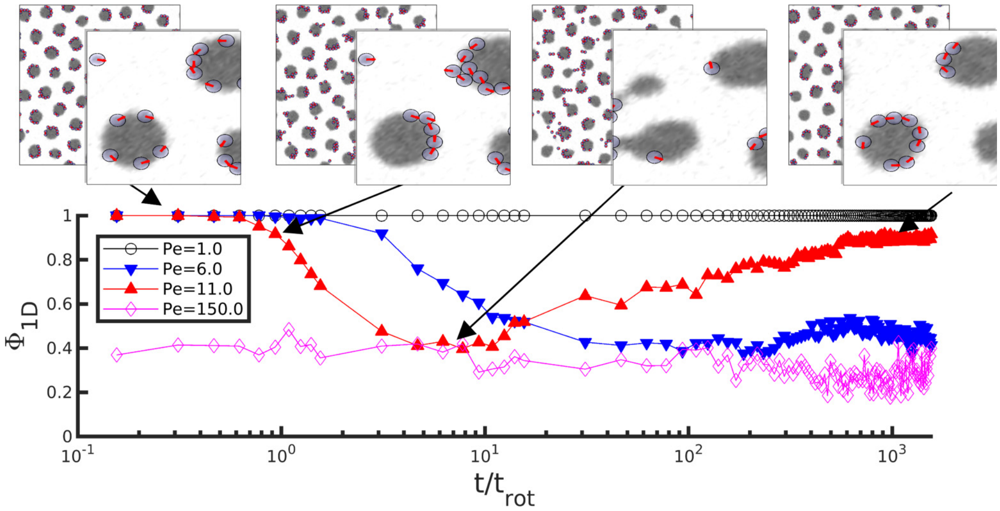

FIG. 3. Dynamic behavior of the fraction of 1D AP clusters for four representative activities corresponding to the four regimes identified in Fig. 2. The system is initialized at $t = 0$ with APs at the interface of equilibrated circle-forming BCP domains. The curves can be compared with Fig. S4 [47] for an initially random condition.

BCP [48]. Figure 4 displays several relevant coassembled regimes for particle-polymer and particle-colloid alignment, $g_{cpl} = 34.9$ and $g_{cc} = 0.06$, when APs are compatible with the minority phase and concentrate in the circular domains. The confinement strength $\tilde{\epsilon}_{cpl}$, which decreases with Pe, determines the ability of APs to deform the confining domains. At low Pe, passivelike APs display no ordering, marked in black circles. As the activity grows, the self-propulsion leads to APs accumulating at the domain walls, where they experience a torque promoting tangential alignment to the interfaces. Such an accumulation occurs when APs self-propel before decorrelating their orientation for a length l_{pers} comparable to the diameter of the BCP domains (see Fig. S6 [47]).

For small concentrations, the interface-particle coupling torque dominates, leading to the flow of APs along the interfaces. As a result, polarized 1D trainlike clusters displace along the interface, while softly confined within the circular phase, marked as red upside triangles. In this regime the interface coupling remains high enough to prevent APs from penetrating the interface. Similarly, vortices of APs under confinement have been shown for active filaments in deformable vesicles [29] or under geometric confinement [24,27,49,50].

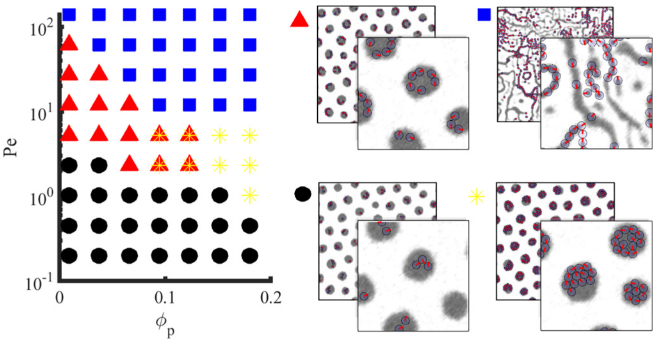

FIG. 4. Phase behavior of selective APs. APs align with respect to BCP interfaces with $g_{cpl} = 34.9$ and $g_{cc} = 0.06$. Markers indicate the different morphologies: Disordered APs within minority domains are marked as black circles, chain/ring structures are marked with red triangles, close-packed structures within minority domains are marked as yellow asterisks, and free particles are marked as blue squares.

For higher concentrations, $\phi_p > 0.09$, crowding in the BCP domains limits the APs' ability to form trainlike polarized clusters. As a result, two-dimensional clusters are preferentially formed. This regime is marked with yellow asterisks, which overlap with the trainlike vortices, indicating their coexistence. In this regime APs can considerably deform the equilibrium BCP domain shape while APs can accumulate forming caps, in a similar way as described for active filaments [29].

At higher activities, APs can escape the soft confinement, marked as blue squares, and form swarms with internal polar ordering, similar to the ones shown in Fig. 2. Contrary to neutral APs, selective ones do not acquire global polar order, which can be attributed to neutral APs promoting flat interfaces. Higher concentrations reduce the required Pe to allow APs to escape the soft confinement. In this regime, the BCP and AP timescales are largely decoupled because the AP swimming timescale is considerably faster than the BCP relaxation time.

The form of the phase diagram for selective APs in Fig. 4 differs from the neutral one in Fig. 2. Specifically, for a fixed concentration, neutral APs form polarized trains and unstructured cluster phases at different Pe, while selective APs display coexistence. This is due to the specific mechanism of reentrance for neutral APs, which leads to APs to explore neighboring domains when they can escape the confining interfaces. Selective APs form train morphologies at smaller Pe, and these morphologies modulate the escape of collective APs at higher Pe, influencing the cluster morphology.

Polarized trainlike morphologies have been found for both neutral and selective APs. The soft confinement induced by the BCP leads to emergent chirality with equally probable clockwise and counterclockwise rotation. The emergence of

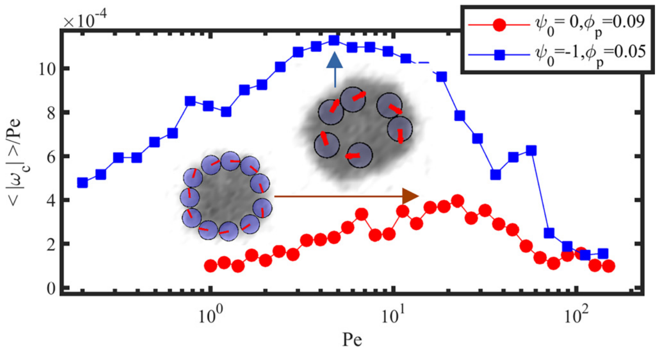

FIG. 5. Mean absolute value of the angular frequency ω_c of APs with neutral ($\psi_0 = 0$, $\phi_p = 0.08$) and selective interactions ($\psi_0 = -1$, $\phi_p = 0.05$) with the BCP mesophase.

chiral motion is found for a wide range of g_{cpl} values as shown in Figs. S8 and S10 [47]. Interestingly, the particle-particle alignment appears to play no role in the emergence of polarised clusters as shown in Figs. S9, S11, and S12 [47]. Figure 5 shows the emergence of collective, in-cluster chiral motion controlled by the BCP mesophase, as quantified by the in-cluster APs' angular velocity ω_c [see Eq. (S28) [47]]. The angular velocity is scaled with Pe in order to concentrate on the cluster morphology contributions to the angular momentum and eliminate the effect of velocity modulus $|\mathbf{v}_i| \propto \mathrm{Pe}$ for $\mathrm{Pe} \gg 1$. Increasing Pe initially promotes the aggregation of APs that triggers the emergence of chiral motion, albeit via a different mechanism depending on the AP affinity. Qualitatively, the BCP confinement is one dimensional for neutral APs and involves APs detaching and reentering BCP interfaces. On the other hand, selective APs undergo two-dimensional confinement, not requiring escaping BCP domains to form train clusters. Therefore, the maximal value of $\langle|\omega_c|\rangle$ occurs for smaller Pe for selective APs. For higher Pe, APs can escape confinement and ω_c decreases as the BCP becomes less able to confine the APs.

APs have been shown to coassemble within BCP melts to produce emergent organized structures displaying a rich phase behavior. This is a consequence of both the BCP intrinsic ordering and the self-propulsion of the APs subject to soft confinement by the BCP. The emergent chiral motion found in this Letter will generalize to 3D spherical morphologies of the BCP, as the active filaments' rotational motion has been shown to be sustained by spherical vesicles [29]. BCP melts constitute a particularly interesting example of a deformable, confining medium with intrinsic ordering at the mesoscale. The use of a coarse-grained, thermodynamically consistent description of the BCP has allowed us to reach the required length scales and timescales characteristic of BCP-AP coassembly. A more microscopic description for the BCP will serve to validate the accuracy of the BCP coarse-grained description under strong forcing, reached at a very high Pe.

The authors thank the European Union's Horizon 2020 Research and Innovation Programme project VIMMP under Grant Agreement No. 760907. I.P. acknowledges support from Ministerio de Ciencia, Innovación y Universidades MCIU/AEI/FEDER for financial support under Grant Agreement No. PID2021-126570NB-100 AEI/FEDER-EU, and from Generalitat de Catalunya under Program Icrea Acadèmia, and Project No. 2021SGR-673.

---

[1] F. S. Bates and G. H. Fredrickson, Annu. Rev. Phys. Chem. **41**, 525 (1990).
[2] M. W. Matsen and F. S. Bates, Macromolecules **29**, 1091 (1996).
[3] R. B. Thompson, Science **292**, 2469 (2001).
[4] B. J. Kim, J. Bang, C. J. Hawker, J. J. Chiu, D. J. Pine, S. G. Jang, S.-M. Yang, and E. J. Kramer, Langmuir **23**, 12693 (2007).
[5] E. Ploshnik, A. Salant, U. Banin, and R. Shenhar, Phys. Chem. Chem. Phys. **12**, 11885 (2010).
[6] E. Ploshnik, A. Salant, U. Banin, and R. Shenhar, Adv. Mater. **22**, 2774 (2010).
[7] E. Ploshnik, K. M. Langner, A. Halevi, M. Ben-Lulu, A. H. E. Müller, J. G. E. M. Fraaije, G. J. Agur Sevink, and R. Shenhar, Adv. Funct. Mater. **23**, 4215 (2013).
[8] J. Huh, V. V. Ginzburg, and A. C. Balazs, Macromolecules **33**, 8085 (2000).
[9] A. Halevi, S. Halivni, M. Oded, A. H. E. Müller, U. Banin, and R. Shenhar, Macromolecules **47**, 3022 (2014).
[10] J. Tailleur and M. E. Cates, Phys. Rev. Lett. **100**, 218103 (2008).
[11] M. E. Cates and J. Tailleur, Annu. Rev. Condens. Matter Phys. **6**, 219 (2015).
[12] V. Telezki and S. Klumpp, Soft Matter **16**, 10537 (2020).
[13] B. t. Hagen, S. van Teeffelen, and H. Löwen, J. Phys.: Condens. Matter **23**, 194119 (2011).
[14] P. Romanczuk, M. Bär, W. Ebeling, B. Lindner, and L. Schimansky-Geier, Eur. Phys. J.: Spec. Top. **202**, 1 (2012).
[15] M. E. Cates and J. Tailleur, Europhys. Lett. **101**, 20010 (2013).
[16] Y. Fily and M. C. Marchetti, Phys. Rev. Lett. **108**, 235702 (2012).
[17] G. S. Redner, M. F. Hagan, and A. Baskaran, Phys. Rev. Lett. **110**, 055701 (2013).
[18] J. Bialké, H. Löwen, and T. Speck, Europhys. Lett. **103**, 30008 (2013).
[19] P. Digregorio, D. Levis, A. Suma, L. F. Cugliandolo, G. Gonnella, and I. Pagonabarraga, Phys. Rev. Lett. **121**, 098003 (2018).
[20] C. Bechinger, R. Di Leonardo, H. Löwen, C. Reichhardt, G. Volpe, and G. Volpe, Rev. Mod. Phys. **88**, 045006 (2016).
[21] G. Frangipane, G. Vizsnyiczai, C. Maggi, R. Savo, A. Sciortino, S. Gigan, and R. Di Leonardo, Nat. Commun. **10**, 2442 (2019).
[22] C. C. Lakey and M. S. Turner, Artif. Life Robot. **27**, 218 (2022).
[23] A. Bricard, J.-B. Caussin, D. Das, C. Savoie, V. Chikkadi, K. Shitara, O. Chepizhko, F. Peruani, D. Saintillan, and D. Bartolo, Nat. Commun. **6**, 7470 (2015).
[24] E. Lushi, H. Wioland, and R. E. Goldstein, Proc. Natl. Acad. Sci. USA **111**, 9733 (2014).
[25] J. P. Hernandez-Ortiz, C. G. Stoltz, and M. D. Graham, Phys. Rev. Lett. **95**, 204501 (2005).

[26] X. Yang, M. L. Manning, and M. C. Marchetti, Soft Matter **10**, 6477 (2014).
[27] H. Wioland, F. G. Woodhouse, J. Dunkel, J. O. Kessler, and R. E. Goldstein, Phys. Rev. Lett. **110**, 268102 (2013).
[28] K. Kruse, J. F. Joanny, F. Jülicher, J. Prost, and K. Sekimoto, Phys. Rev. Lett. **92**, 078101 (2004).
[29] M. S. Peterson, A. Baskaran, and M. F. Hagan, Nat. Commun. **12**, 7247 (2021).
[30] L. Angelani and R. D. Leonardo, New J. Phys. **12**, 113017 (2010).
[31] S. A. Mallory, C. Valeriani, and A. Cacciuto, Phys. Rev. E **90**, 032309 (2014).
[32] H. H. Wensink, V. Kantsler, R. E. Goldstein, and J. Dunkel, Phys. Rev. E **89**, 010302(R) (2014).
[33] M. A. Fernandez-Rodriguez, F. Grillo, L. Alvarez, M. Rathlef, I. Buttinoni, G. Volpe, and L. Isa, Nat. Commun. **11**, 4223 (2020).
[34] X. Wang, M. In, C. Blanc, M. Nobili, and A. Stocco, Soft Matter **11**, 7376 (2015).
[35] X. Wang, M. In, C. Blanc, P. Malgaretti, M. Nobili, and A. Stocco, Faraday Discuss. **191**, 305 (2016).
[36] Q. Yang and K. Loos, Macromol. Chem. Phys. **218**, 1600451 (2017).
[37] Q. Yang and K. Loos, Polym. Chem. **8**, 641 (2017).
[38] J. Diaz, M. Pinna, A. Zvelindovsky, and I. Pagonabarraga, Soft Matter **15**, 6400 (2019).
[39] J. Diaz, M. Pinna, A. V. Zvelindovsky, and I. Pagonabarraga, Polymers **14**, 1910 (2022).
[40] T. Ohta and K. Kawasaki, Macromolecules **19**, 2621 (1986).
[41] H. Tanaka and T. Araki, Phys. Rev. Lett. **85**, 1338 (2000).
[42] T. Vicsek, A. Czirók, E. Ben-Jacob, I. Cohen, and O. Shochet, Phys. Rev. Lett. **75**, 1226 (1995).
[43] E. Sesé-Sansa, I. Pagonabarraga, and D. Levis, Europhys. Lett. **124**, 30004 (2018).
[44] L. S. Palacios, J. Katuri, I. Pagonabarraga, and S. Sánchez, Soft Matter **15**, 6581 (2019).
[45] J. W. Cahn, J. Chem. Phys. **30**, 1121 (1959).
[46] J. W. Cahn and J. E. Hilliard, J. Chem. Phys. **31**, 688 (1959).
[47] See Supplemental Material at http://link.aps.org/supplemental/10.1103/PhysRevE.108.L062601 for a full description of the model and additional simulation results, which includes Refs. [51–54].
[48] B. J. Kim, J. Bang, C. J. Hawker, and E. J. Kramer, Macromolecules **39**, 4108 (2006).
[49] F. G. Woodhouse and R. E. Goldstein, Phys. Rev. Lett. **109**, 168105 (2012).
[50] K.-T. Wu, J. B. Hishamunda, D. T. N. Chen, S. J. DeCamp, Y.-W. Chang, A. Fernández-Nieves, S. Fraden, and Z. Dogic, Science **355**, eaal1979 (2017).
[51] H. E. Cook, Acta Metall. **18**, 297 (1970).
[52] R. C. Ball and R. L. H. Essery, J. Phys.: Condens. Matter **2**, 10303 (1990).
[53] I. W. Hamley, Macromol. Theory Simul. **9**, 363 (2000).
[54] M. Pinna and A. V. Zvelindovsky, Eur. Phys. J. B **85**, 210 (2012).